

The rate and contribution of mergers to mass assembly from NIRC*am* observations of galaxy candidates up to 13.3 billion years ago

Nicolò Dalmasso^{1,2} , Antonello Calabrò³, Nicha Leethochawalit⁴, Benedetta Vulcani⁵ , Kristan Boyett^{1,2}, Michele Trenti^{1,2} , Tommaso Treu⁶ , Marco Castellano³, Maruša Bradač^{7,8} , Benjamin Metha^{1,2}, Paola Santini³ 

¹*School of Physics, University of Melbourne, Parkville, Vic 3010, Australia*

²*Australian Research Council Centre of Excellence for All-Sky Astrophysics in 3-Dimensions, Australia*

³*INAF Osservatorio Astronomico di Roma, Via Frascati 33, 00078 Monteporzio Catone, Rome, Italy*

⁴*National Astronomical Research Institute of Thailand (NARIT), Mae Rim, Chiang Mai, 50180, Thailand*

⁵*INAF Osservatorio Astronomico di Padova, vicolo dell'Osservatorio 5, 35122 Padova, Italy*

⁶*Department of Physics and Astronomy, University of California, Los Angeles, 430 Portola Plaza, Los Angeles, CA 90095, USA*

⁷*University of Ljubljana, Department of Mathematics and Physics, Jadranska ulica 19, SI-1000 Ljubljana, Slovenia*

⁸*Department of Physics and Astronomy, University of California, Davis, 1 Shields Ave, Davis, CA 95616, USA*

Accepted XXX. Received YYY; in original form ZZZ

ABSTRACT

We present an analysis of the galaxy merger rate in the redshift range $4.0 < z < 9.0$ (i.e. about 1.5 to 0.5 Gyr after the Big Bang) based on visually identified galaxy mergers from morphological parameter analysis. Our dataset is based on high-resolution NIRC*am* JWST data (F150W and F2000W broad-band filters) in the low-to-moderate magnification ($\mu < 2$) regions of the Abell 2744 cluster field. From a parent set of 675 galaxies ($M_{UV} \in [-26.6, -17.9]$), we identify 64 merger candidates from the Gini, M_{20} and Asymmetry morphological parameters, leading to a merger fraction $f_m = 0.11 \pm 0.04$. There is no evidence of redshift evolution of f_m even at the highest redshift considered, thus extending well into the epoch of reionization the constant trend seen previously at $z \lesssim 6$. Furthermore, we investigate any potential redshift dependent differences in the specific star formation rates between mergers and non-mergers. Our analysis reveals no significant correlation in this regard, with deviations in the studied redshift range typically falling within 0.25 dex (logarithmic scale) that can be attributed to sample variance and measurement errors. Finally, we also demonstrate that the classification of a merging system is robust with respect to the observed (and equivalently rest-frame) wavelength of the high-quality JWST broad-band images used. This preliminary study highlights the potential for progress in quantifying galaxy assembly through mergers during the epoch of reionization, with significant sample size growth expected from upcoming large JWST infrared imaging datasets.

Key words: galaxies: high-redshift – galaxies: structure – galaxies: interactions – galaxies: star formation

1 INTRODUCTION

Interactions between galaxies critically influence their physical properties and play a core role in their mass accumulation and growth, driving morphological transformations and often resulting in mergers (Toomre & Toomre 1972). The role of interactions and mergers is pivotal to our understanding of galaxy evolution, including how their impact may change over cosmic time. One key measurement is the fraction of the galaxy population undergoing a merger, denoted as merger fraction (f_m), and whether there is any dependence with redshift or on galaxy properties, such as stellar mass or luminosity.

Direct imaging studies of the galaxy merger fraction broadly fall into two main methodologies; (i) examining the frequency of galaxies in close proximity to estimate upcoming mergers (“close pair identification method”, e.g., Barnes 1988; Le Fèvre et al. 2000; Patton et al. 2002; Schmidt et al. 2013) and (ii) measuring the morphology

of individual sources to identify ongoing/recently completed mergers (“morphological parameters method”, e.g., Conselice et al. 2003; Lotz et al. 2008a; Conselice et al. 2009; Conselice & Arnold 2009).

Over the last two decades, investigations beyond the local Universe have predominantly utilized Hubble Space Telescope (HST) imaging. Lotz et al. (2008b) used the All-Wavelength Extended Groth Strip International Survey (AEGIS) to study galaxy morphologies and merger frequencies over the redshift range $0.2 < z < 1.2$ and determined a merger fraction consistent with no redshift evolution; measuring $f_m = 0.10 \pm 0.02$ using a parent sample with $I_{F814W} < 25.0$. This was supported by Conselice et al. (2009), who identified a consistent merger fraction of $f_m \sim 0.10$ for galaxies between redshifts $0.6 < z < 1.2$ using both Extended Groth Strip (EGS) (Davis et al. 2007) and The Cosmic Evolution Survey (COSMOS) (Scoville et al. 2007) surveys.

However, studies of massive (stellar mass $M_* > 10^{10} M_\odot$) galaxies lying on the star-forming main sequence (hereafter MS) at $0.2 < z < 2.0$ identified an increase in the merger fraction with

* e-mail: ndalmasso@student.unimelb.edu.au

increasing redshift; from $f_m \sim 0.03$ at $z \sim 0.5$ to $f_m \sim 0.13$ at $z \sim 1.5$ (Speagle et al. 2014; Cibinel et al. 2019). Additionally, these investigations found a dependence of the merger fraction on galaxy properties, with the likelihood of galaxies merging depending significantly on their distance from the MS. In a similar redshift interval of $0.3 < z < 2.5$, examining late-stage mergers from the CANDELS/3DHST catalog (identified using a peak-finding algorithm), the findings presented in Silva et al. (2018) emphasize a heightened star formation rate (SFR) for mergers with stellar masses $M_* > 10^{10} M_\odot$ compared to the MS.

Kim et al. (2021) also determined a redshift evolution in the merger fraction in a mass-selected galaxy sample ($9.0 < \log(M/M_\odot) < 11.5$) in the North Ecliptic Pole-Wide field using the morphological parameters of the candidates to detect mergers. Within their sample, they obtained a merger fraction of $f_m \in (0.10, 0.20)$ at $z < 0.6$, consistent with Conselice et al. (2009), with a marginally higher fraction of $f_m \sim 0.20$ for galaxies in the redshift range $4.0 < z < 6.0$, consistent with the high mass sample ($10^9 M_\odot$) from Conselice & Arnold (2009) at the same epoch and with the same merger identification method.

Moreover, Ventou et al. (2017, 2019) examined the evolution of the merger fraction out to $z = 6$ using the close pair identification method with data collected from MUSE (the Multi-Unit Spectroscopic Explorer) and determined that the evolution of the merger fraction is best described by two distinct behaviors. In the local Universe, they observed a significant decline in the merger fraction with cosmic time reaching the lower limit of $f_m = 0.009 \pm 0.02$ at redshift $z = 0.05$ (De Propriis et al. 2007). However, for redshift greater than $z \sim 1$, the major merger fraction remained approximately constant at a value of around $f_m \sim 0.1$. These findings are not only consistent with observational measurements, such as those in Conselice et al. (2009), but also with simulations, including ILLUSTRIS (Snyder et al. 2017) and EMERGE (O’Leary et al. 2021), especially when considering a sample of galaxies with a stellar mass $M_* \geq 10^{9.5} M_\odot$. Importantly, none of these studies suggest an increase in the merger fraction beyond $z > 2$.

Significantly, investigations into the merger fraction using conventional methodologies, primarily relying on ground-based observatories and the Hubble Space Telescope, have been confined to redshifts $z < 6$ due to the limited availability of high-resolution deep near-infrared (NIR) imaging and wavelength filters crucial for directly examining the rest-optical structures of high-redshift galaxies. However, with the advent of the James Webb Space Telescope (JWST), we can now expand the study of morphological characteristics and parameters of galaxies to higher redshifts, leveraging the enhanced sensitivity of the Near Infrared Camera (NIRCam) instrument. Recent studies have demonstrated the potential to utilize improvements in resolution and wavelength availability afforded by JWST observational filters (e.g., Treu et al. 2023; Vulcani et al. 2023; Tohill et al. 2024).

Notably, recent studies, not solely based on observational data, have transcended standard methodologies of identifying mergers by employing random forest (RF) and Machine Learning classifications trained on simulated JWST images from CEERS and the IllustrisTNG simulation, achieving accuracies of approximately 60% (Rodríguez-Gomez et al. 2019; Snyder et al. 2019; Rose et al. 2023). These alternative methods have been utilized to measure the merger fraction and observe redshift evolution, revealing a transition from $f_m \sim 0.03$ at $z \sim 0.7$ to $f_m \sim 0.40$ at $z \sim 3.7$ (Rose et al. 2023). This highlights significant deviations from studies using standard methods and underscores that the identification method of galaxy mergers at high redshifts holds the potential to introduce substantial systematic ef-

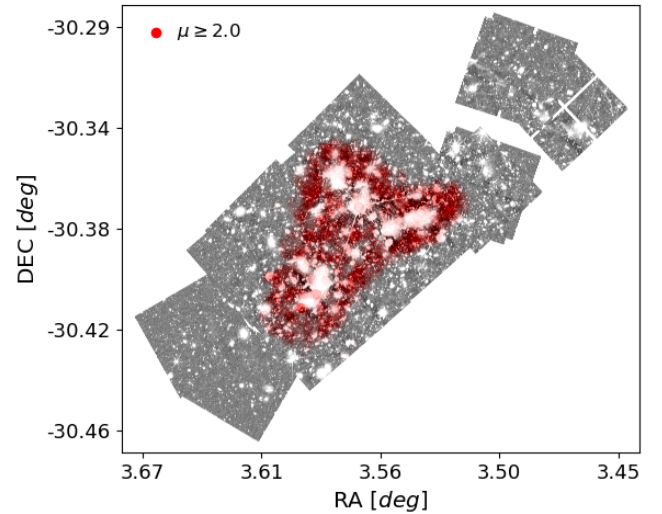


Figure 1. NIRCcam scientific map in the F150W filter. The red region represents the area where the magnification is $\mu \geq 2.0$. The galaxies detected in this region are excluded from the sample.

fects.

In this study we conduct a comprehensive study of galaxy mergers in the epoch of reionization by leveraging the deep NIRCcam imaging from the GLASS-JWST ERS program (Treu et al. 2022), UNCOVER JWST-GO-2561 (Bezanson et al. 2022) and DDT-2756 (PI Wenlei Chen). These new observations provide us with the opportunity to extend the morphological studies out to redshift $z \sim 9$ (lookback time of about 13.3 Gyr), and offer a more extensive dataset in comparison to prior studies that relied on HST data. Our study focuses on the low-magnification regions in the outskirts of galaxy cluster Abell 2744, where we employ morphological statistical parameters to assess the prevalence of merger systems across a wide range of redshifts. Our objective is to extend the investigation of galaxy mergers to the high redshift, a domain that has not been thoroughly explored before, encompassing both bright and faint galaxies out to $z \sim 9$.

The structure of this paper is organized as follows: Sec.2 provides a comprehensive overview of the data selection process for the galaxy candidates. In Sec.3, we outline the galaxy morphological parameters and merger criteria that we will employ to identify interacting systems. In Sec.4 we determine the merger fraction and then examine and discuss any redshift evolution within our sample and whether there are any galaxy characteristics differences between mergers and non-mergers (e.g. the sSFR). Finally, in Sec.5, we provide a summary of our discoveries. In App.A, we present a study exploring the influence of observation filter wavelengths on the analysis of morphological parameters.

In this work we assume, when relevant, a standard cosmology with $H_0 = 70 \text{ km s}^{-1} \text{ Mpc}^{-1}$, $\Omega_m = 0.3$, $\Omega_\Lambda = 0.7$. Magnitudes are in the AB system (Oke & Gunn 1983).

2 OBSERVATIONAL DATA AND SAMPLE SELECTION

The NIRCcam imaging data used in this study were obtained through three public programs focused on the foreground galaxy cluster Abell 2744 and its immediate surroundings: (i) GLASS JWST-ERS-1324 (Treu et al. 2022), (ii) UNCOVER JWST-GO-2561 (Bezanson et al. 2022), and (iii) the Director’s Discretionary Time Program 2756 (PI

NIRCam observations				
$z - \text{bin}$	N_g	\bar{z}	M_{UV}	$\log_{10}(M_*/M_\odot)$
(1)	(2)	(3)	(4)	(5)
$4.0 \leq z < 5.0$	845(319)	4.50	[−26.6, −17.9]	[6.9, 11.4]
$5.0 \leq z < 6.0$	1333(186)	5.34	[−24.7, −18.3]	[7.2, 10.9]
$6.0 \leq z < 7.0$	386(107)	6.47	[−23.1, −18.5]	[7.3, 9.9]
$7.0 \leq z < 8.0$	414(30)	7.47	[−23.6, −18.7]	[7.6, 10.7]
$8.0 \leq z < 9.0$	250(33)	8.50	[−25.6, −19.3]	[7.5, 12.4]

Table 1. Summary of the galaxies used in this work for mergers identification, obtained using data JWST NIRCam data from the GLASS Collaboration. The sources are selected as discussed in Sec.2. (1) Redshift bin. (2) Number of galaxies detected.. (3) Mean redshift of the subsample. (4) Absolute UV Magnitude range of the subsample. (5) Stellar mass range. Quantities in columns (3), (4) and (5) are referred to the subsamples used in this work in **bold** (2).

Wenlei Chen). We use the publicly available galaxy and photometric catalogs for the combined footprint of these three programs, as provided by Merlin et al. (2022); Paris et al. (2023) with the photometric redshifts estimated by fitting the full HST+JWST photometry to Bruzual & Charlot (2003) templates by means of the zPHOT code (Fontana et al. 2000), using the same technique adopted in Santini et al. (2023). Additionally, we employ the high-resolution reduction (hereafter referred to as hres, with 1 pixel = 0.02") of the F150W and F200W NIRCam imaging by Brammer (2023) over the entire survey area, as illustrated in Fig.1.

Because we focus on a high redshift sample of galaxies, we restrict the Paris et al. (2023) source catalog to candidates with a photometric redshift in the range of $4 \leq z < 9$. We set an upper bound at $z = 9$ due to the low number of candidates at such a high redshift, limiting any statistical constraints we can place on our population analysis. This provides an initial catalogue of 3228 galaxies. To ensure we can robustly measure the morphological parameters, we imposed both a signal-to-noise ratio (SNR) and a star class requirements, demanding that candidate galaxies in the observed NIRCam imaging bands exhibit a total SNR exceeding $SNR = 7.0$ in each band and star class value of `class_star` < 0.9.

Additionally, for our morphological analysis we aim to ensure that the parameters we measure reflect the true shape of the galaxies and are not deformed by gravitational lensing, which is important in our study because our NIRCam footprint includes the Abell 2744 galaxy cluster. We considered the impact of gravitational lensing and opted to exclude regions with excessively high magnification coefficients. Galaxies were deemed suitable if their median magnification, computed by Bergamini et al. (2023), fell below $\mu < 2.0$. Fig.1 illustrates the region excluded by this criterion, highlighted in red.

Finally, to ensure the completeness of our sample, we implement an apparent magnitude cutoff, making a conservative assumption using the limiting AB magnitude at 5σ for NIRCam in the F150W band (rest-frame UV 1500-3000Å for our sample), which was set at $m_{AB} = 28.87$. Absolute UV magnitudes at 1500Å and stellar masses were calculated by fitting the photometry with Bruzual & Charlot (2003) templates and assuming a delayed exponentially declining SFH, as done in Santini et al. (2023).

Tab.1 shows the number of candidates detected by NIRCam (total: 3228) in each redshift bin and the number of targets after the application of the selection criteria used in this work (total: 675).

Given that the angular-diameter distance is relatively constant at high z , to conduct morphological parameters estimations for each galaxy we consider a cutout from the composite high-resolution map (with 1 pixel = 0.02") of 110px on a side corresponding to 2.2" on a side (our science images are drizzled on a 0.02"/pixel scale).

3 ANALYSIS

3.1 Morphological Parameter Definition

In this work we employ three widely recognized quantitative morphological statistics, employed for characterization of mergers: the Gini coefficient (G), the second-order moment of brightness (M_{20}), and the asymmetry (A , see Conselice 2014). The definitions are given below for convenience of the reader and to set the notation¹.

The Gini coefficient, proposed as a morphological parameter by Abraham et al. (2003), quantifies the inequality in the distribution of pixel intensities within a galaxy image. It is computed as:

$$G = \frac{1}{\bar{X}n(n-1)} \sum_i^n (2i - n - 1)X_i \quad (1)$$

where X_i represents the intensity of the i^{th} pixel, n is the total number of pixels assigned to the galaxy from the segmentation map, and \bar{X} is the mean intensity. By definition, this parameter falls within the range of $[0, 1]$, where a value of 0 implies that the galaxy exhibits a uniform distribution in terms of intensity, while a value of 1 indicates that one pixel possesses all the flux. For galaxy mergers, it is anticipated that this morphological parameter will be higher compared to non-mergers. This expectation arises from the fact that the process of galaxy mergers often results in a more concentrated distribution of light within the merged system. This concentration occurs due to interactions between galaxies and the central concentration of stellar material, contributing to a higher value of this parameter (e.g., Lotz et al. 2008a).

The second-order moment of brightness M_{20} , introduced by Lotz et al. (2004), measures the compactness and concentration of the brightest 20% of a galaxy's light. It is defined as:

$$M_{20} = \log_{10} \left(\frac{\sum_i M_i}{M_{\text{tot}}} \right), \quad \text{with } \sum_i f_i < 0.2 f_{\text{tot}} \quad (2)$$

where f_{tot} is the total flux of the galaxy pixels identified by the segmentation map, M_i is the second-order moment of brightness for each pixel, and $M_{\text{tot}} = \sum_i^n M_i = \sum_i^n f_i \left[(x_i - x_c)^2 + (y_i - y_c)^2 \right]$, with f_i being the single pixel intensities, x_i and y_i are the pixel coordinates, while x_c and y_c correspond to the galaxy center where M_{tot} is minimized. Typical values for this parameter are typically found in the range of $[-3, 0]$. Increasing values within this range are correlated with a greater number of off-centered bright features associated with

¹ The morphological parameters were measured using JWSTmorph, a publicly accessible code available on the GitHub repository: <https://github.com/Anthony96/JWSTmorph.git>

the galaxy under study. The merger process tends to make the central region of the merging galaxies more concentrated and brighter. Consequently, this concentration has a significant impact on the M_{20} parameter. Non-merging galaxies, on the other hand, typically exhibit a smoother and less concentrated distribution of bright pixels, resulting in lower M_{20} values. These galaxies may lack the distinct, compact, and bright regions that are characteristic of merging systems, M_{20} is expected to be higher for galaxy mergers compared to non-mergers.

The asymmetry parameter (A), proposed by Abraham et al. (1996) and Conselice et al. (2000), is calculated as:

$$A = \frac{\sum |I - I_\pi|}{\sum I} - A_{\text{bkg}}, \quad (3)$$

where I is the original cutout image, I_π is the image rotated by 180 degrees (or π radians), and A_{bkg} denotes the asymmetry of the background. By construction, the asymmetry parameter tends to be higher for galaxy mergers compared to non-mergers. This is because mergers usually disrupt structures, introduce asymmetry and irregularities into a galaxy's appearance.

These morphological parameters are measured using hres image cutouts of the candidates selected in Sec.2 using JWSTmoprh. The segmentation maps, which are used to assign the pixels to a galaxy, are derived as in Treu et al. (2022) through the *photutils* package² (Bradley et al. 2023), using a threshold flux for detection of 2σ above the background.

3.2 Identifying Mergers

The morphological parameters described above can be used to classify whether a galaxy is a merger, and Conselice et al. (2003) and Lotz et al. (2008a) set out merger criteria using the two equations:

$$f(G, M_{20}) = G + 0.14M_{20} > 0.33 \quad (4)$$

$$A \geq 0.35 \quad (5)$$

These two equations have been derived from HST observations and have been validated for lower redshifts, extending only up to $z \sim 1.2$. It is worth noting that this redshift range falls considerably short of our intended investigation, which targets galaxies at $z \geq 4$. Nevertheless, recent research (Treu et al. 2023; Vulcani et al. 2023) has revealed minimal variations in the underlying parameters with respect to redshift. In light of these findings, we proceed to employ these equations in our examination of our galaxy sample. To facilitate classification, we introduce two distinct samples:

- Silver (S): galaxies that satisfy the first criteria Eq.4 are classified as members of the Silver sample.
- Gold (G): galaxies that satisfy both criteria equations Eq.4 and Eq.5 are classified as members of the Gold sample.

By employing these classification criteria, we are able to categorize mergers based on their adherence to specific conditions, enabling a more systematic analysis of merger populations in the field of astrophysics (Lotz et al. 2008a).

In Fig.2, we offer a representative example of galaxies categorized as mergers and non-mergers in each redshift bin. The upper row showcases a non-merger candidate, while the lower row presents a merger candidate, the associated morphological parameters are presented as a reference.

² <https://photutils.readthedocs.io/en/stable/citation.html>

4 RESULTS AND DISCUSSION

4.1 Mergers characterization

We measure the morphological parameters for the 675 galaxies in our parent sample, and use these to define a Silver and Gold sub-sample of mergers based on our merger criteria. We measure these parameters from the hres imaging, and note that we find consistent values for the structural parameters and merger classifications when using alternative filters (see App.A). Our classification outcomes are visually depicted in Fig.3, where the two dashed lines represent the threshold values derived from Eq.4 and 5. Each data point on the graph corresponds to an individual galaxy from our sample, chosen based on the criteria detailed in Sec.2 and summarized in Tab.1.

Fig.4 provides the respective count of galaxies falling into each region defined by the dashed lines in Fig.3. The blue circle represents the total sample of galaxies that meet the selection criteria outlined in Sec.2, the brown circle designates the Silver sample, while the red circle represents the Gold sample.

To offer a more comprehensive characterization of the candidate sample selected for this study and the identified mergers, we additionally present two figures. Fig.5 shows the galaxy absolute magnitude in U-band (left panel) and stellar mass (right panel) as a function of redshift for the Gold sample and the non-merger galaxies (all the galaxies excluded from the Gold sample). It is apparent that the two distinct categories of galaxies, i.e., mergers and non-mergers, exhibit a comparable range in terms of both magnitude and mass, so we can state that mergers are not typically brighter or more massive than isolated galaxies (to 2σ) and this inference is valid across the whole redshift range of our analysis. Furthermore, for a spatial perspective and to better visualize the distribution of classified mergers, Fig.6 displays the F150W image in (RA, DEC) coordinates. Overlaid on the image are galaxies classified as mergers (Gold sample) and those that do not fall into this category. This visualization is based on high-resolution data and covers the entire redshift range, specifically $z \in [4.0, 9.0]$.

4.2 Merger fraction versus redshift

In each redshift bin, we define the merger fraction $f_{m,i}$ as the number of mergers (N_i) over the total number of galaxies (N_{tot}) in the bin:

$$f_{m,i} = \frac{N_i}{N_{\text{tot}}}. \quad (6)$$

Additionally, to examine if there is any merger fraction trend with magnitude, we implement a magnitude cutoff to divide the sample into bright and faint galaxies. We set a magnitude threshold at $M_U = -20.1$, the median of all galaxies presented in the left panel of Fig.5.

We apply a similar approach when creating two sub-samples by introducing a stellar mass cutoff for the candidates, with a threshold of $\log(M/M_\odot) = 8.5$. This threshold corresponds to the median of all galaxies presented in the right panel of Fig.5.

In Fig.7, we depict the merger fraction across the redshift range, considering both the Gold and Silver samples examined in this study. We present the merger fraction f_m in the top two panels when considering the total sample of galaxies, alongside two sub-samples created by implementing a magnitude cutoff to distinguish them. The two lower panels show the same quantity, but this time, the sample is segregated based on stellar mass.

The distinction in defining these two samples has a noticeable impact on the overall merger fraction across all the redshifts

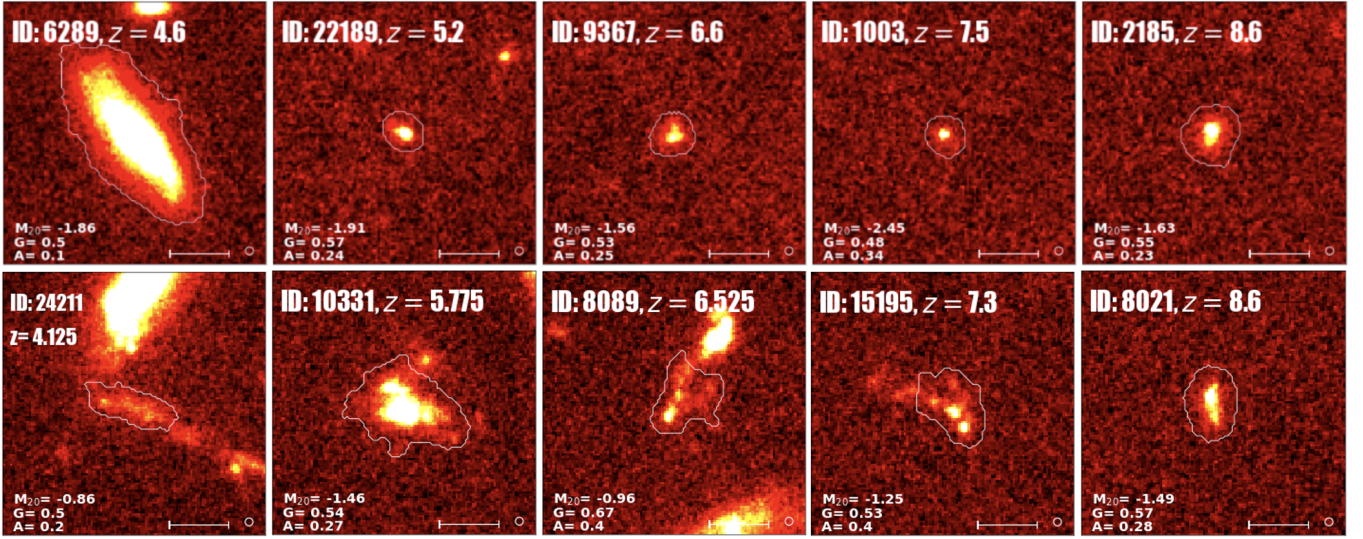


Figure 2. Illustrative representations from various redshift ranges, featuring extracted cutouts alongside corresponding morphological metrics, ID and photometric redshift. These snapshots are derived from a composite hres map (20mas per pixel), integrating data from F150W and F200W bands. The upper row highlights non-merging galaxies, while the lower row presents merger candidates. Each cutout stamp is $2.2''$ on a side, while the horizontal bar is $0.5''$ wide.

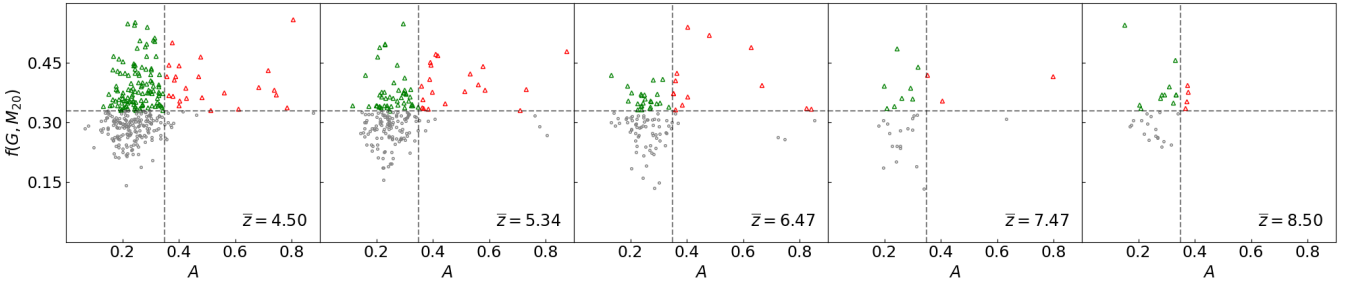


Figure 3. Visual representation of the classical classification method presented in Section 3.2. The two dashed lines represent the two classification thresholds of a merger Eq.4 and Eq.5, in four different z -bins. The galaxies marked by triangles (in both green and red) represent those classified as mergers in the Silver sample. The subset identified as mergers in the Gold sample is highlighted in red.

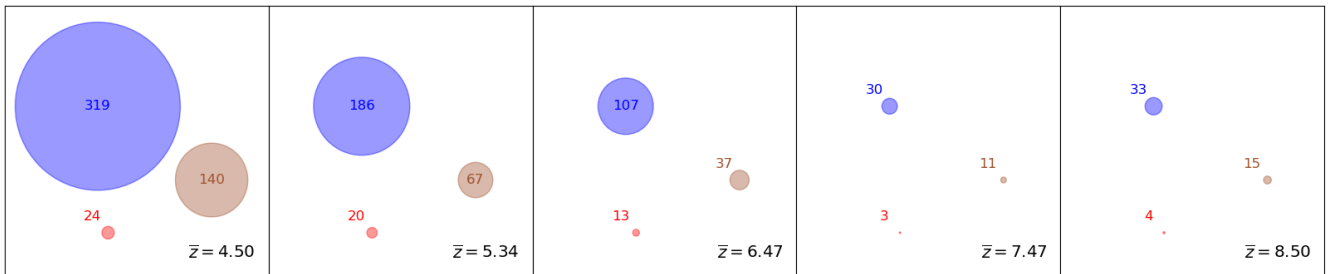


Figure 4. Visual representation of the demography of the different samples, obtained from the merger classification equations (Eq.4 and Eq.5), in different redshift bins, as indicated in the bottom right corners. Blue color indicates the total sample size, brown color indicates the Silver sample composed by the galaxies that meets the Eq.4 (green and red triangles in Fig.3); and red color show the Gold sample constituted by the galaxies that satisfy both the merger classification criteria.

considered in our study. This effect is visually evident in Fig.4 when we look at the number of galaxies in each group. When we consider our entire sample (blue regions in Fig.7) we observe minimal variation with redshift in the measured merger fraction with redshift for our Silver and Gold criteria. Specifically, for the Silver sample, the merger fraction is measured to be $f_m = 0.39 \pm 0.06$ when considering the entire redshift range. In contrast, the Gold sample exhibits a substantially lower of $f_m = 0.11 \pm 0.04$. The

choice between the Silver and Gold samples has a significant impact on the derived merger fraction values. While the Silver sample, with its more permissive criteria, yields higher merger fractions across the redshift range, the Gold sample, which employs stricter criteria, results in consistently lower and more stable merger fractions.

Our assessments of merger fractions based on Gold-criteria identification reveal no discernible redshift evolution, with an f_m value consistent with findings from lower redshift investigations.

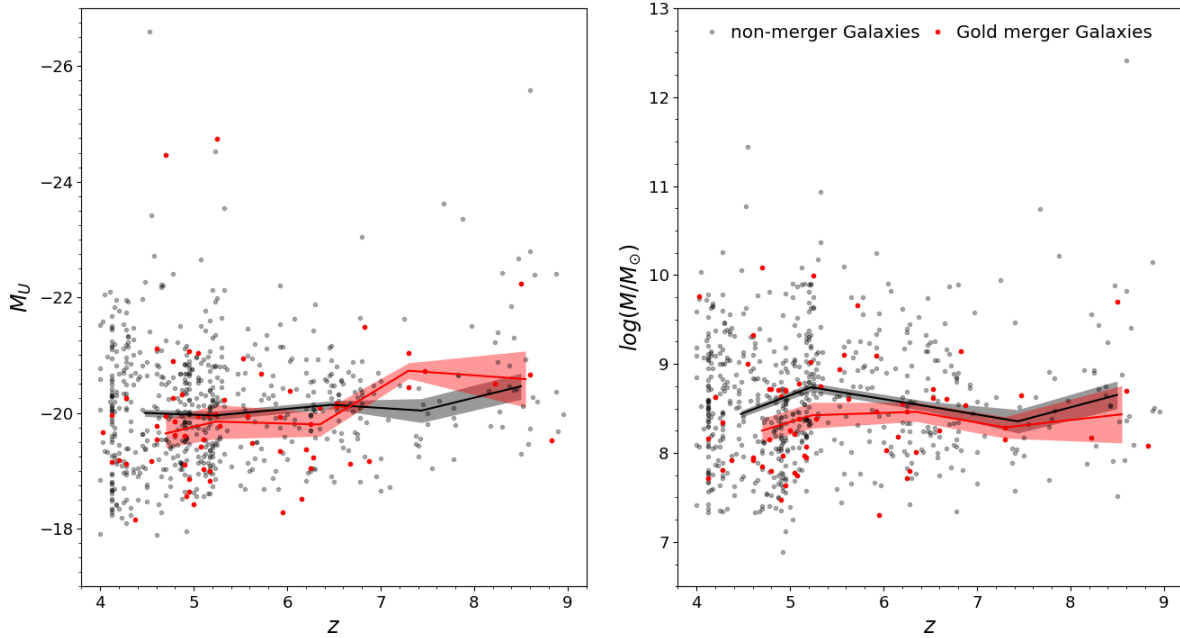


Figure 5. Rest frame U-magnitude (left) and stellar mass (right) as a function of photometric redshift for the Gold sample (red) and for all other, non-merger galaxies (grey). Solid lines represent the corresponding median evolution with redshift of the two different samples of mergers and non-mergers. Shaded regions represent the standard error corresponding to these median values.

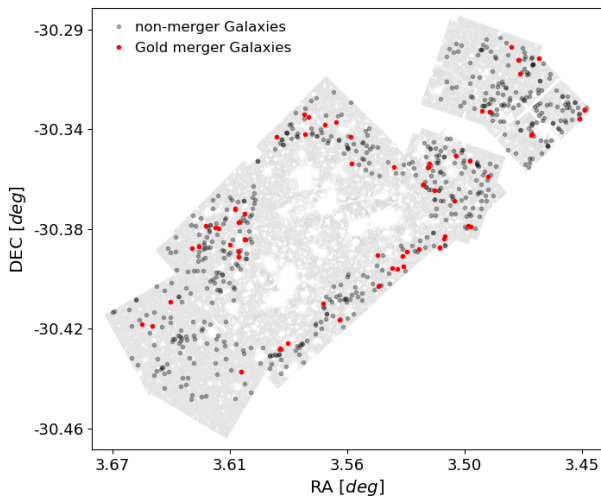


Figure 6. The Gold sample merger and non-merger obtained in all the different redshift bins considering only the high-resolution band. This image therefore refers to the identified mergers coloured in blue in Fig.3. Note that the central region is not populated as we have adopted a cut in magnification equal to $\mu < 2.0$, Fig.1.

This alignment with prior research in the field lends additional credence to the proposition that the merger fraction exhibits negligible dependence on redshift. Earlier investigations (e.g. Lotz et al. 2008a; Lin et al. 2008; Conselice et al. 2009; López-Sanjuan

et al. 2009; Jogee et al. 2009; Kim et al. 2021) focused on galaxies at lower redshifts $z < 1.2$. These studies consistently observed that the merger fraction tends to exhibit a relatively stable pattern around the value of $f_m \sim 0.10$, showing no significant overarching trend in relation to redshift. Our results align also with studies conducted at higher redshifts (e.g., Ventou et al. 2017, 2019) which also suggest that beyond a certain redshift threshold, likely below $z < 1$, the merger fraction remains constant around a value of $f_m \sim 0.10$ and does not display significant fluctuations. As a result, there is no noticeable upward or downward trend in the merger fraction among subsamples of galaxies meeting our selection criteria, which includes those with stellar masses of $M_* \geq 10^{8.5} M_\odot$.

4.3 sSFR of interacting and non-interacting systems

We aim to explore potential variations in the impact of galaxy mergers on specific star formation activity across distinct redshifts.

To derive the star formation rates, we use BAGPIPES (Carnall et al. 2018) to fit the photometries of the galaxies. BAGPIPES' model galaxy spectra were generated with a Kroupa et al. (2022) initial mass function, a Calzetti et al. (2000) dust attenuation law, a BPASS (V2.2.1 Eldridge & Stanway 2009) stellar population, and nebular emission lines from CLOUDY photoionization code (Ferland et al. 2017). For the fit, we set the metallicity range to $[0, 1.2] Z_\odot$, the dust attenuation A_V to $[0, 3]$ mag, the logarithm of the ionization parameter U to $[-4, -1]$, and the logarithm of the total mass of stars formed in solar mass to $[6, 13]$. We assumed two star formation histories: log-normal and non-parametric forms (Iyer et al. 2019).

We partition the visual dataset of galaxies into four distinct subsets: two distinguished by mass and two by magnitude, with classifications of merger (Gold sample) and non-merger (all galaxies outside the Gold sample). To ensure consistency with the threshold outlined in Sec.4.2, we adopt identical threshold values. Specifically, the thresh-

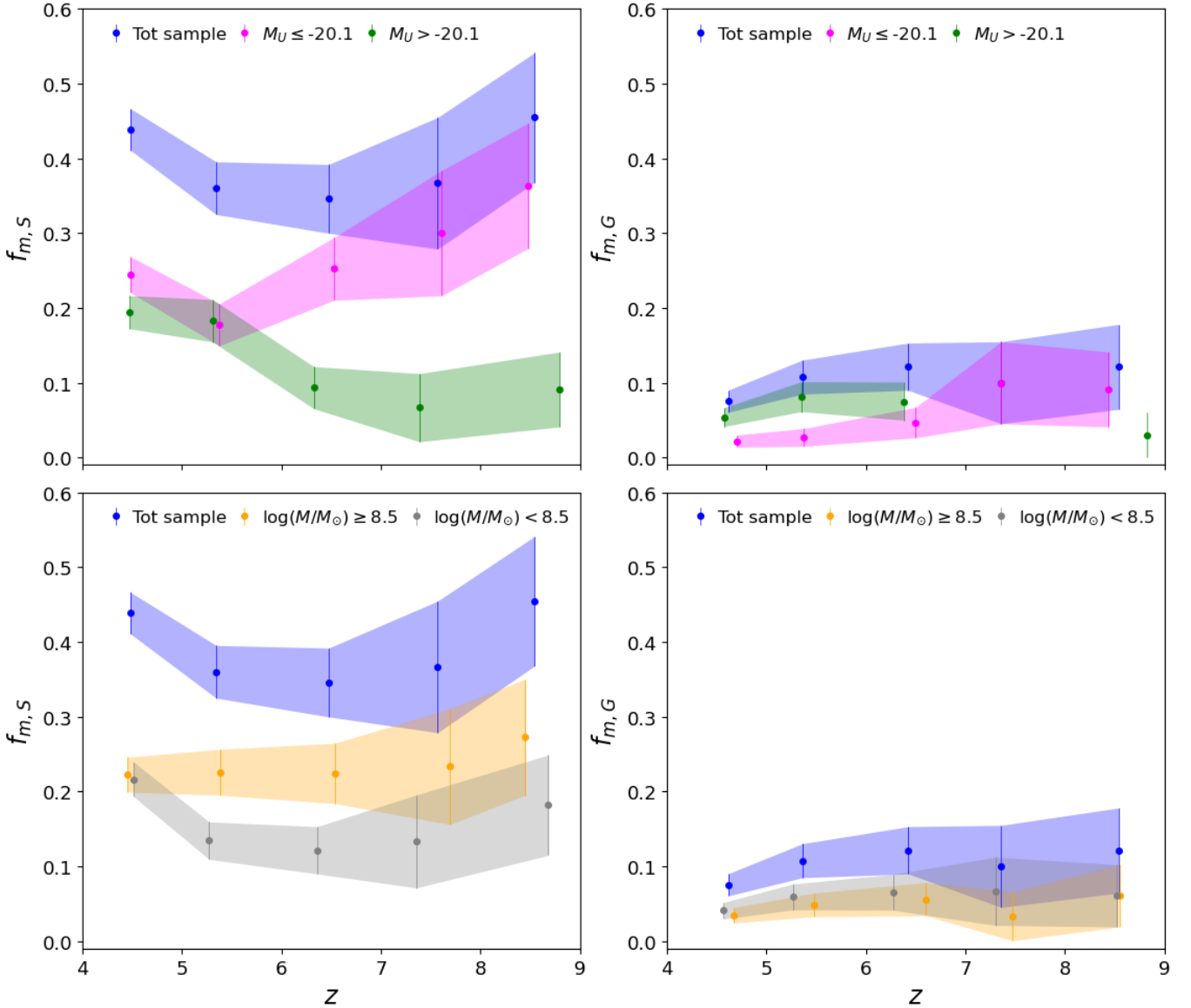


Figure 7. Merger fraction of the Silver sample (left panels) and of the Gold sample (right panels) as a function of redshift. The definition of the fraction follows the equation Eq.6. In the top panels, we show a further separation based on the rest frame magnitude, with bright galaxies classified as having U-band magnitudes below $M_{U,th} = -20.1$, and faint galaxies lying above this threshold. In the bottom panels, we separate galaxies into a high mass sample ($M_* > 10^{8.5} M_\odot$) and a low mass sample ($M_* < 10^{8.5} M_\odot$).

old for absolute magnitude was established at $M_U = -20.1$, while for mass, it was $\log_{10}(M/M_\odot) = 8.5$. We utilize a metric representing the excess of specific star formation rate (sSFR) for galaxies classified as mergers in comparison to non-mergers. This excess is calculated using the equation:

$$\Delta \log(\text{sSFR}_i) = \log(\langle \text{sSFR}_{\text{merger}} \rangle_i) - \log(\langle \text{sSFR}_{\text{non-merger}} \rangle_i) \quad (7)$$

where (i) represents the specific redshift bin being examined, the associated standard error is used to address uncertainties.

According to the definition, values of $\Delta \log(\text{sSFR}) > 0$ indicate that galaxies identified as mergers within a specific subset of data, categorised based on criteria such as magnitude or mass, exhibit a higher rate of star formation per unit mass compared to galaxies classified as non-mergers. Therefore, these measurements would suggest that candidates within this particular subset are currently ex-

periencing heightened levels of star formation relative to a reference or baseline. Conversely, data points falling below the zero baseline ($\Delta \log(\text{sSFR}) < 0$) indicate subsets of merger events where the sSFR is lower than what we observe in galaxies classified as non-mergers.

In Fig. 8, we present our findings within the redshift range $4.0 \leq z < 7.0$, a selection motivated by a noticeable decrease in statistical significance for $z \geq 7.0$ within the parent sample (blue and red circles in Fig.4). The data points resulting from the analysis of all subsamples, along with the entire catalog of mergers and non-mergers (depicted in blue), are closely distributed around the zero level, denoted by a black dashed line.

The oscillations with respect to the zero line are contained within 0.25 dex on a logarithmic scale across all the redshift range studied, these result suggest that there is no compelling evidence of any significant (positive or negative) excess in the sSFR for mergers when compared to non-mergers.

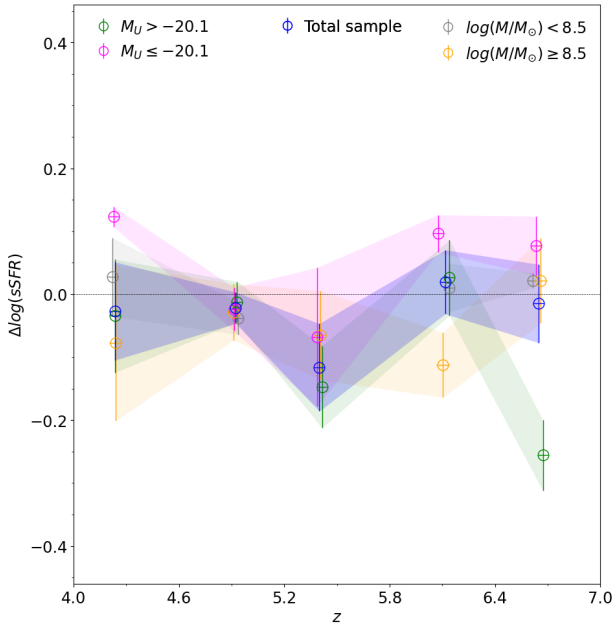


Figure 8. Evolution of the excess specific star formation rate (sSFR) of the Gold sample, Eq.7, as a function of redshift. We present the evolution for four different subsamples of galaxies, for both mass and magnitude threshold values we used the same ones as in Sec.4.2, in addition we overplot the evolution of the same quantity when considering the entire sample of galaxy mergers and non-mergers.

5 SUMMARY AND PERSPECTIVES

In this study, we focus on high- z galaxies in the outskirts (low magnification regions) of the foreground galaxy cluster Abell 2744, observed as part of the GLASS-JWST program ERS-1324 (Treu et al. 2022), UNCOVER JWST-GO-2561 (Bezanson et al. 2022) and DDT-2756 (PI Wenlei Chen).

Our main objective was to use high-resolution ($1\text{px} = 0.02''$) F150W and F200W imaging to conduct an in-depth analysis of the evolution of the merger fraction f_m with respect to redshift, extending from $z = 4$ up to $z \approx 9$. We accomplished this by investigating various subsamples, which were derived based on magnitude and mass thresholds. Our key findings are as follows:

- We investigated morphological parameters for high-redshift galaxies, categorizing them into two distinct merger subsamples: Silver and Gold. We employed the criteria outlined in Eq.4 and Eq.5, as defined in prior research on this topic. Our results are depicted in Fig.3, illustrating the distribution of morphological parameters, and in Fig.4, which provides a visual representation of the number of candidates in each sample, correlated with the mean redshift of the candidates within the selected bins.

- In order to obtain a more comprehensive understanding of the merger population in comparison to non-interacting galaxies, we have provided visual representations of the magnitude and mass distributions in Fig.5. These distributions have been segregated between candidates identified as Gold mergers and all galaxies included in the study, adhering to the selection criteria outlined in Sec.2. It is worth noting that no distinct trends have emerged from our analysis. We have observed that mergers are present across the entire range of magnitudes and masses at different redshifts. Notably, the distributions of these two categories exhibit similarities,

as indicated by the medians of both magnitude and mass.

- Fig.7 displays the evolution of the merger fraction of two separate subsamples for various magnitude and mass ranges. The overall sample, represented by the blue contours, shows relatively small variations in the merger fraction, making it challenging to discern a significant trend. Notably, for the Gold sample, the values remain stable across the entire range of redshifts under investigation. The calculated mean value, along with its associated error, is $f_m = 0.11 \pm 0.04$. This outcome aligns with previous research at lower redshifts, as cited in (Lotz et al. 2008a; Lin et al. 2008; Conselice et al. 2009; López-Sanjuan et al. 2009; Jogee et al. 2009; Kim et al. 2021), all of which indicated a merger fraction oscillating around $f_m \sim 0.10$. Our result is also supported by studies up to redshift $z = 6$, such as Ventou et al. 2017 and Ventou et al. 2019, which reported a consistent trend of the merger fraction, remaining around the same value found at low redshift of $f_m \sim 0.10$ for massive galaxies in line with our sample having $M_* \geq 10^{8.5} M_\odot$. In light of these results, it is reasonable to suggest that the merger fraction does not display strong dependencies on redshift. This conclusion extends the findings obtained at lower redshifts, where Treu et al. (2023); Vulcani et al. (2023) argue that morphological parameters, which form the basis for classifying mergers and non-mergers and subsequently calculating the merger fraction, do not exhibit a strong dependence on the redshift at which galaxies are observed.

- Our study aimed to investigate potential differences in the star formation rate between two categories: mergers and non-mergers. As illustrated in Fig. 8, we do not observe a clear and robust trend in the specific star formation rate for mergers compared to non-interacting galaxies, with redshift as the independent variable. Between low and high redshift of $4.5 < z < 6.5$ the oscillations are contained in 0.25 dex around the zero line with no clear increasing or decreasing trend.

- There is no apparent correlation between the identification of mergers according to the wavelengths of the observation filters utilized to establish the initial sample. Consequently, the merger fraction does not display any specific pattern in this aspect maintaining a level around $f_m \sim 0.10$ across the examined redshift range, consistent with prior literature and the primary finding of this study.

To go beyond the preliminary results for the merger fraction during the initial stages of the epoch of reionization, further data is required. To improve statistical robustness and address potential cosmic variance effect (Trenti & Stiavelli 2008) as well as any weak-magnification lensing bias, a promising prospective strategy involves examining galaxies and images across diverse fields (e.g., COSMOS (Scoville et al. 2007), EGS (Davis et al. 2007), PRIMER (Dunlop et al. 2021)), in addition to those considered in this work. This will enable a thorough exploration of the galactic environment, incorporating factors such as metallicity and spatial density and open opportunities to quantitative comparison to predictions from numerical simulations and theoretical modelling of galaxy assembly in the first billion years.

ACKNOWLEDGEMENTS

This research was supported by the Australian Research Council Centre of Excellence for All Sky Astrophysics in 3 Dimensions (ASTRO 3D), through project number CE170100013. This work is based on observations made with the NASA/ESA/CSA James Webb Space Telescope. The data were obtained from the Mikulski Archive for Space Telescopes at the Space Telescope Science Institute,

which is operated by the Association of Universities for Research in Astronomy, Inc., under NASA contract NAS 5-03127 for JWST. These observations are associated with programs JWST-ERS-1324, JWST-GO-2561, and JWST-DDT-2756. BV acknowledges support from the INAF Large Grant 2022 “Extragalactic Surveys with JWST” (PI Pentericci). MB acknowledges support from the ERC Advanced Grant FIRSTLIGHT and Slovenian national research agency ARRS through grants N1-0238 and P1-0188. BM acknowledges support from the Australian Government Research Training Program (RTP) Scholarship.

DATA AVAILABILITY

The data used to conduct the analysis are from: (i) GLASS JWST-ERS-1324 [Treu et al. \(2022\)](#), (ii) UNCOVER JWST-GO-2561 [Bezanson et al. \(2022\)](#), and (iii) the Director’s Discretionary Time Program 2756 (PI Wenlei Chen). Photometric catalog provided by [Merlin et al. 2022](#); [Paris et al. 2023](#).

REFERENCES

- Abraham R. G., Tanvir N. R., Santiago B. X., Ellis R. S., Glazebrook K., Bergh S. v. d., 1996, *Monthly Notices of the Royal Astronomical Society*, 279, L47
- Abraham R. G., van den Bergh S., Nair P., 2003, *The Astrophysical Journal*, 588, 218
- Barnes J. E., 1988, *ApJ*, 331, 699
- Bergamini P., et al., 2023, *ApJ*, 952, 84
- Bezanson R., et al., 2022, *arXiv e-prints*, p. arXiv:2212.04026
- Bradley L., et al., 2023, *astrophy/photutils*: 1.8.0, doi:10.5281/zenodo.7946442, <https://doi.org/10.5281/zenodo.7946442>
- Brammer G., 2023, *grizli*, Zenodo, doi:10.5281/zenodo.1146904
- Bruzual G., Charlot S., 2003, *MNRAS*, 344, 1000
- Calzetti D., Armus L., Bohlin R. C., Kinney A. L., Koornneef J., Storchi-Bergmann T., 2000, *ApJ*, 533, 682
- Carnall A., McLure R., Dunlop J., Davé R., 2018, *Monthly Notices of the Royal Astronomical Society*, 480, 4379
- Cibinel A., et al., 2019, *MNRAS*, 485, 5631
- Conselice C. J., 2014, *ARA&A*, 52, 291
- Conselice C. J., Arnold J., 2009, *MNRAS*, 397, 208
- Conselice C. J., Bershady M. A., Jangren A., 2000, *The Astrophysical Journal*, 529, 886
- Conselice C. J., Bershady M. A., Dickinson M., Papovich C., 2003, *The Astronomical Journal*, 126, 1183
- Conselice C. J., Yang C., Bluck A. F. L., 2009, *Monthly Notices of the Royal Astronomical Society*, 394, 1956
- Davis M., et al., 2007, *ApJ*, 660, L1
- De Propriis R., Conselice C. J., Liske J., Driver S. P., Patton D. R., Graham A. W., Allen P. D., 2007, *ApJ*, 666, 212
- Dunlop J. S., et al., 2021, PRIMER: Public Release IMaging for Extragalactic Research, JWST Proposal. Cycle 1, ID. #1837
- Eldridge J. J., Stanway E. R., 2009, *MNRAS*, 400, 1019
- Ferland G. J., et al., 2017, *Rev. Mex. Astron. Astrofis.*, 53, 385
- Fontana A., D’Odorico S., Poli F., Giallongo E., Arnouts S., Cristiani S., Moorwood A., Saracco P., 2000, *The Astronomical Journal*, 120, 2206
- Iyer K. G., Gawiser E., Faber S. M., Ferguson H. C., Kartaltepe J., Koekemoer A. M., Pacifici C., Somerville R. S., 2019, *ApJ*, 879, 116
- Jogee S., et al., 2009, *The Astrophysical Journal*, 697, 1971
- Kim E., et al., 2021, *Monthly Notices of the Royal Astronomical Society*, 507, 3113
- Kroupa P., et al., 2022, *MNRAS*, 517, 3613
- Le Fèvre O., et al., 2000, *MNRAS*, 311, 565
- Lin L., et al., 2008, *ApJ*, 681, 232
- López-Sanjuan C., et al., 2009, *ApJ*, 694, 643
- Lotz J. M., Primack J., Madau P., 2004, *The Astronomical Journal*, 128, 163
- Lotz J. M., Jonsson P., Cox T. J., Primack J. R., 2008a, *Monthly Notices of the Royal Astronomical Society*, 391, 1137
- Lotz J. M., et al., 2008b, *The Astrophysical Journal*, 672, 177
- Merlin E., et al., 2022, *The Astrophysical Journal Letters*, 938, L14
- O’Leary J. A., Moster B. P., Naab T., Somerville R. S., 2021, *MNRAS*, 501, 3215
- Oke J. B., Gunn J. E., 1983, *ApJ*, 266, 713
- Paris D., et al., 2023, *The Astrophysical Journal*, 952, 20
- Patton D. R., et al., 2002, *ApJ*, 565, 208
- Rodriguez-Gomez V., et al., 2019, *MNRAS*, 483, 4140
- Rose C., et al., 2023, *The Astrophysical Journal*, 942, 54
- Santini P., et al., 2023, *ApJ*, 942, L27
- Schmidt K. B., et al., 2013, *MNRAS*, 432, 285
- Scoville N., et al., 2007, *The Astrophysical Journal Supplement Series*, 172, 38
- Silva A., et al., 2018, *ApJ*, 868, 46
- Snyder G. F., Lotz J. M., Rodriguez-Gomez V., Guimarães R. d. S., Torrey P., Hernquist L., 2017, *MNRAS*, 468, 207
- Snyder G. F., Rodriguez-Gomez V., Lotz J. M., Torrey P., Quirk A. C. N., Hernquist L., Vogelsberger M., Freeman P. E., 2019, *MNRAS*, 486, 3702
- Speagle J. S., Steinhardt C. L., Capak P. L., Silverman J. D., 2014, *ApJS*, 214, 15
- Tohill C., Bamford S. P., Conselice C. J., Ferreira L., Harvey T., Adams N., Austin D., 2024, *ApJ*, 962, 164
- Toomre A., Toomre J., 1972, *ApJ*, 178, 623
- Trenti M., Stiavelli M., 2008, *ApJ*, 676, 767
- Treu T., et al., 2022, *The Astrophysical Journal*, 935, 110
- Treu T., et al., 2023, *ApJ*, 942, L28
- Ventou E., et al., 2017, *A&A*, 608, A9
- Ventou E., et al., 2019, *Astronomy & Astrophysics*, 631, A87
- Vulcani B., et al., 2023, *ApJ*, 948, L15

APPENDIX A: WAVELENGTH DEPENDENCY STUDY

In this Appendix, we investigate potential correlations between the detection of galaxy mergers and variations in the merger fraction f_m . This examination takes into account the various wavelengths used for candidate identification, utilizing a selection of bands, specifically F200W, F277W, F356W, and F444W, in conjunction with the hres band used as the reference in the main study.

Fig.A1 provides a visualization of the morphological parameters within the same redshift bin and band scheme. Furthermore, Fig.A2 offers a graphical representation of the number of galaxies within the total, Silver, and Gold samples. From these figures, it becomes apparent that there is no significant discrepancy in the number of galaxies detected in each band when examining the same redshift bin. This suggests that there is no pronounced trend in detection based on wavelength.

To further explore potential dependencies, we applied the same magnitude and stellar mass cuts that were considered in the primary study. The goal was to assess whether the wavelength used for the survey impacted the results. Fig.A3 and Fig.A4 present the outcomes of this supplementary analysis. As indicated in these figures, the merger fraction f_m does not exhibit significant fluctuations based on the detection band. Therefore, we conclude that there is no apparent dependency on wavelength. Overall, the results consistently show that the fraction of mergers remains constant, hovering around the value of $f_m \sim 0.10$ across the spectrum of wavelengths studied despite the differences in rest-frame spectral coverage and physical resolution.

In summary, our analysis reveals that there is no discernible increasing or decreasing trend in the merger fraction when considering different detection wavelengths. These results are consistent with the previous findings by [Treu et al. \(2023\)](#), which suggested that the morphology of Lyman Break Galaxies remains relatively consistent across different wavelengths, from the rest frame optical to the rest frame UV.

This paper has been typeset from a $\text{\TeX}/\text{\LaTeX}$ file prepared by the author.

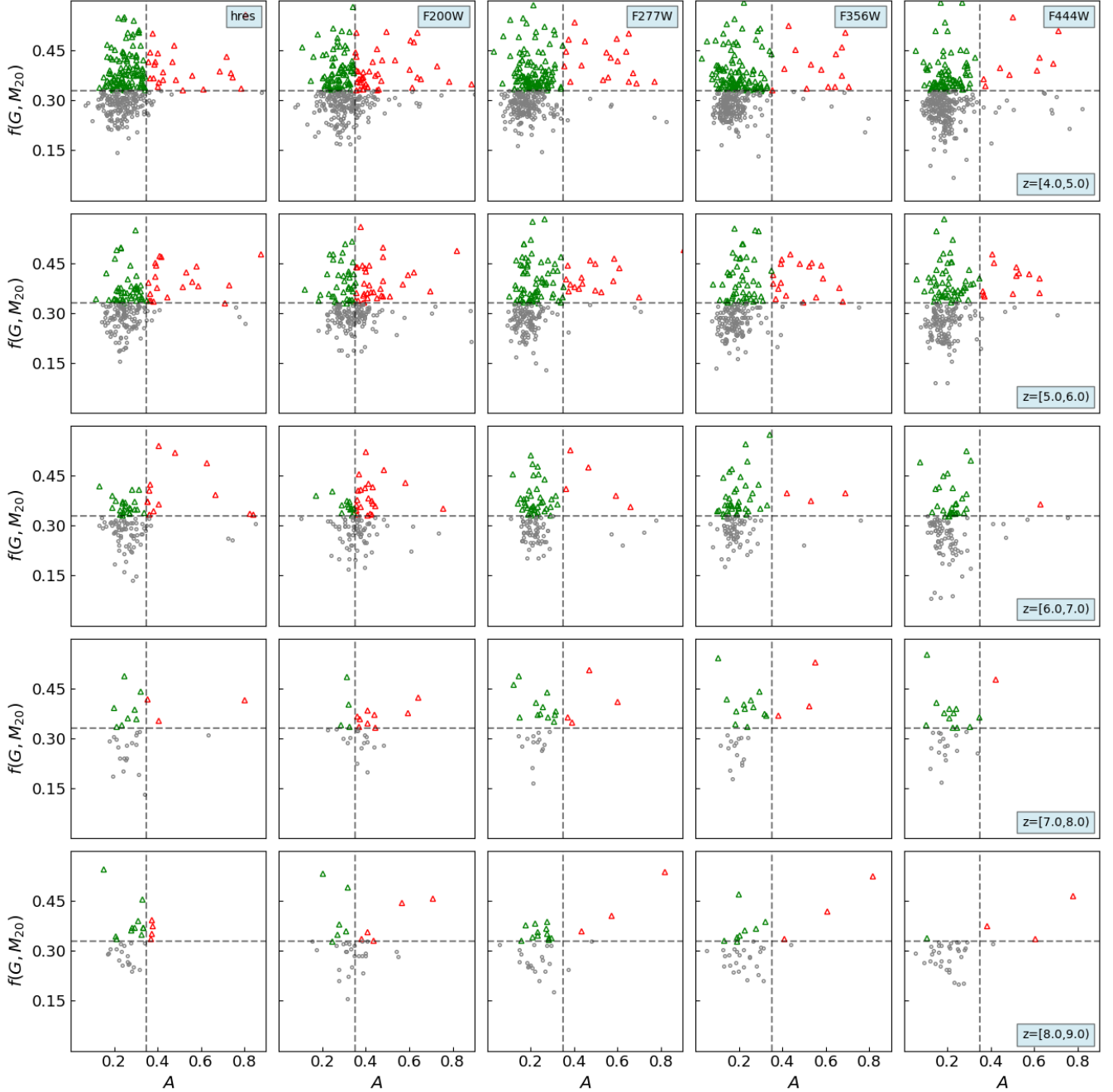


Figure A1. The classical classification method presented in Sec.3.2. Each row shows results for a different redshift bin, with each panel within each row showing results when a different filter is used for determining the morphological parameters. The two dashed lines represent the two classification thresholds of a merger (Eq.4 and Eq.5). In each graph, four regions are created. The galaxies marked by triangles (in both green and red) represent those classified as mergers in the Silver sample. The subset identified as mergers in the Gold sample is highlighted in red. From this plot, we can see that there is not a significant difference in the number of Gold or Silver sample galaxies when different filters are used to compute the morphological parameters (A , G , M_{20}).

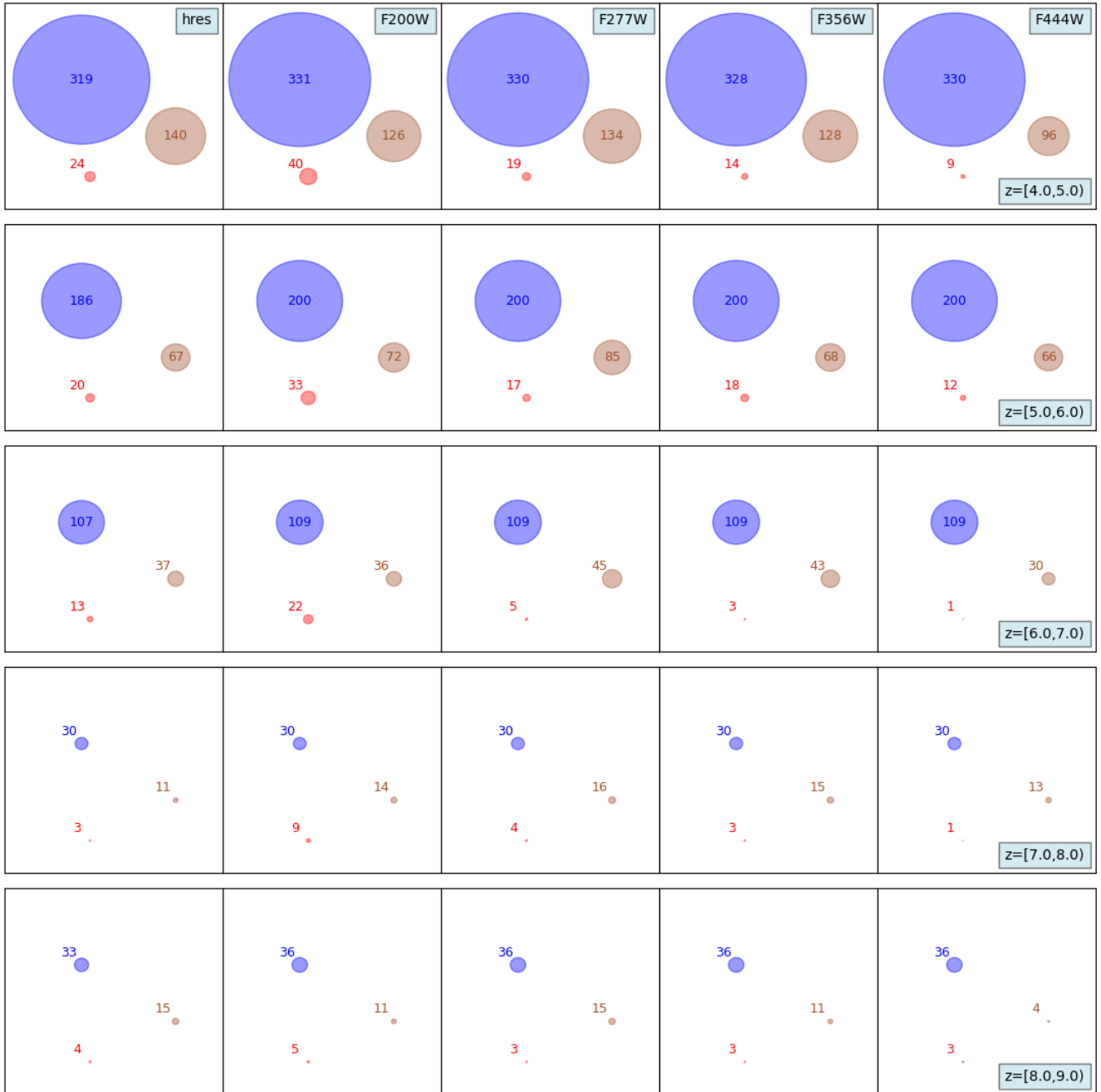


Figure A2. Demographic data on the different samples obtained from the merger classification equations (Eq.4 and Eq.5), formatted in the same way as Fig.A1. Blue color indicates the total sample size, brown color indicates the Silver sample composed by the galaxies that meets the Eq.4 (green and red triangles in Fig.A1); and red color show the Gold sample constituted by the galaxies that satisfy both the merger classification criteria.

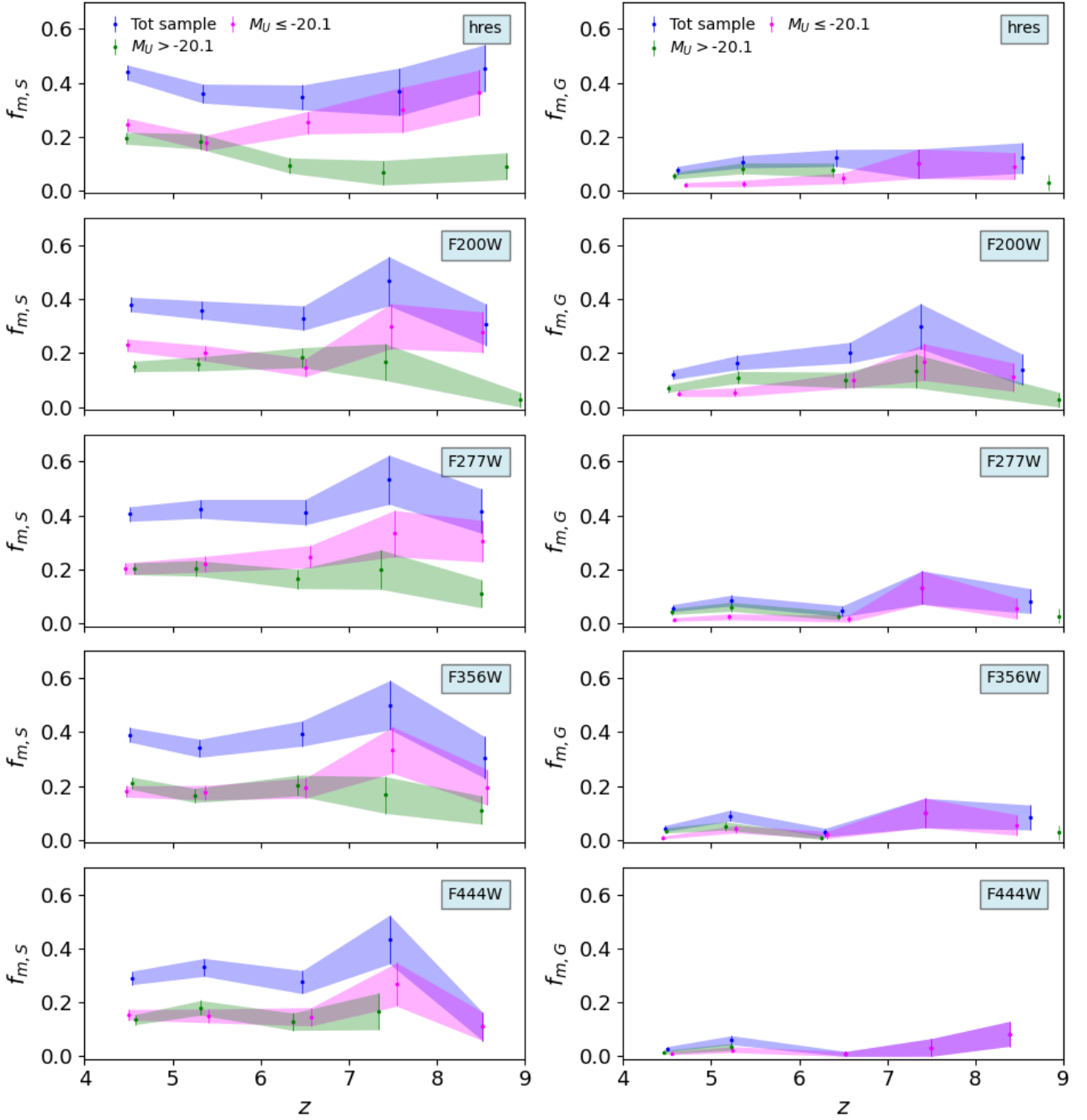


Figure A3. The merger fraction as a function of redshift, using different filters. The left panels show the Silver sample and the right panels represent the Gold sample. Each row shows the results when a different filter is used to identify the Gold and Silver samples. In each panel, we also show the results for the subsamples of bright and faint galaxies, defined by a cut in magnitude at $M_{U,th} = -20.1$.

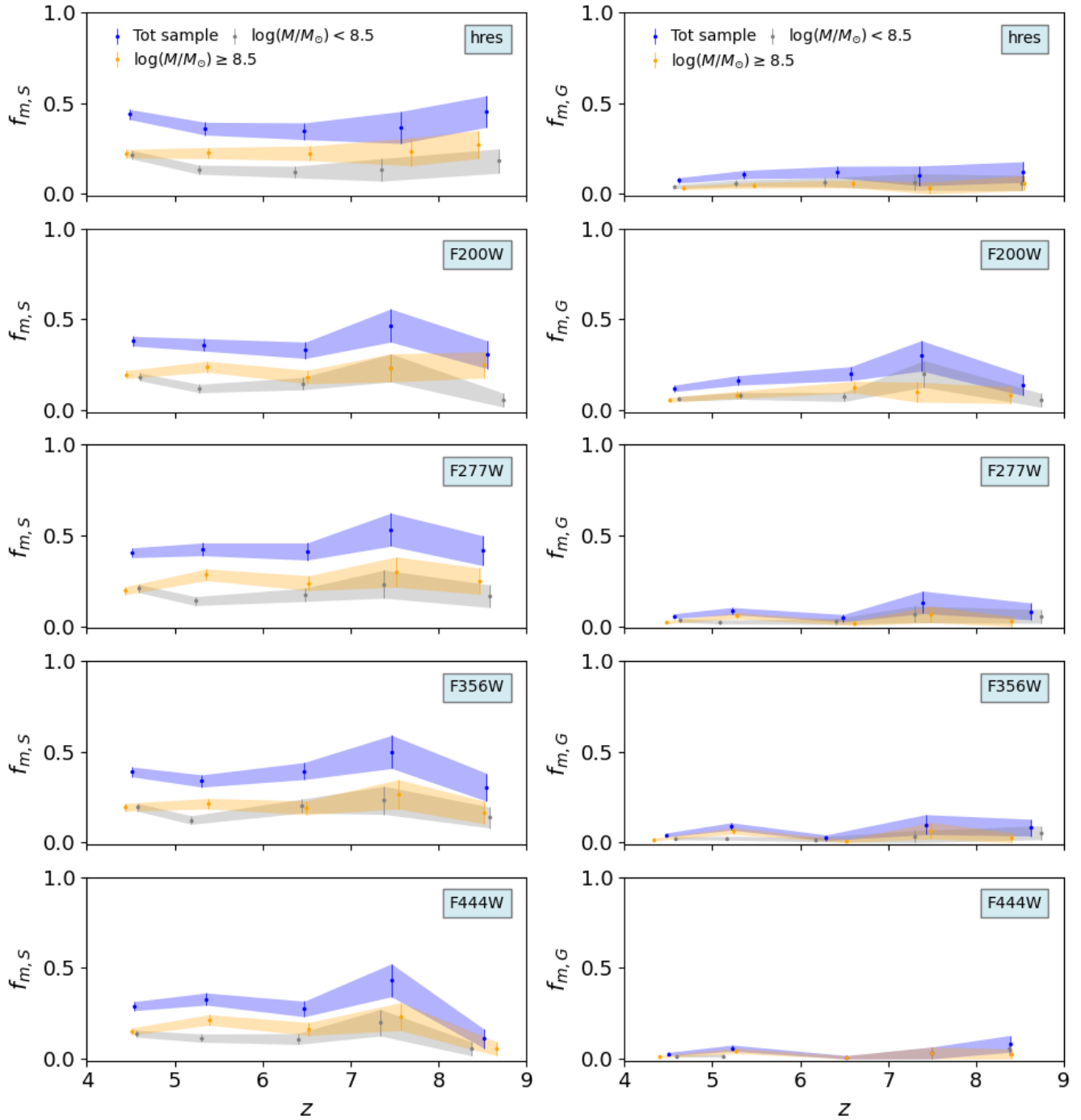


Figure A4. As in Fig. A3, but splitting the total sample into two subsamples based on stellar mass, with high-mass galaxies defined to be those with stellar masses greater than $M_{th} = 10^{8.5} M_{\odot}$, and low-mass galaxies having stellar masses below this value.